Macromolecules

Article

pubs.acs.org/Macromolecules

Alignment and Structural Evolution of Cylinder-Forming Diblock Copolymer Thin Films in Patterned Tapered-Width Nanochannels

Qianqian Tong, Qin Zheng, and S. J. Sibener*

The James Franck Institute and Department of Chemistry, The University of Chicago, 929 E. 57th Street, Chicago, Illinois 60637, United States

ABSTRACT: Control over the orientation of cylindrical block copolymer microdomains and the position of dislocations using tapered nanochannels is herein demonstrated. Dislocations are introduced periodically as the channels become progressively wider. Our high-temperature atomic force microscopy (AFM) enables us to probe real-time and real-space dislocation movement directly. Upon annealing, dislocations are observed to move to their equilibrium positions, where the average free energy of the polymer chains reaches a minimum. Smaller confinement widths impose a powerful guiding field for templating domain alignment, as the deviations of the dislocations at the narrower end of the channel from their equilibrium positions are minimal. Finally, the fluctuations of dislocations across the wedge are studied under different temperatures, and the perpendicular diffusion coefficients and activation energy are determined. These experiments demonstrate the ability to control the placement of periodically located dislocations along tapered nanochannels, offering an efficacious route to placing defects at predetermined locations in such hierarchically assembled nanostructures. This also suggests the possibility of transporting and concentrating defect-seeking species such as nanoparticle additives into intentionally selected locations along the tapered channel.

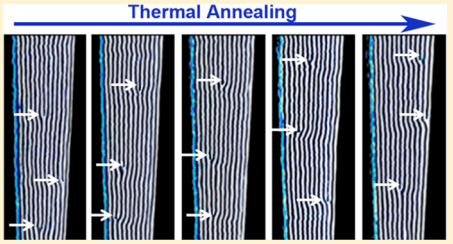

INTRODUCTION

Self-assembled systems have proven to be an attractive fabrication paradigm for nanoscale structures. Diblock copolymers are well-known examples of self-assembling systems. Depending on the molecular weight and the volume fraction of each block, block copolymer thin films spontaneously order into a variety of morphologies, including spheres, cylinders, and lamellea. These self-assembled patterns have been used as nanolithographic masks to create patterns on substrates[1−3] as well as templates for the further synthesis of metallic dots[4,5] and nanowires.[6,7] However, the application of these materials require precise control over the orientation of the polymer domains and formation of long-range ordered nanostructures free from defects. Techniques that have been used to direct the assembly process of block copolymer domains and eliminate defects include electric fields,[8−10] flow fields,[11−13] directional crystallization,[14] chemical patterning,[15−19] and graphoepitaxy.[20−29] Graphoepitaxy utilizes the topography of the substrate to order polymer domains. This technique was first used to achieve long-range order of spherical domains[20−22] and has since been used to align striped patterns of cylinder[23−26,28,29] or lamellae[27] forming block copolymers with both perpendicular and parallel orientations.

For templating of the block copolymer thin films, it is essential to understand the response of the system when the dimensions of the guiding patterns are incommensurate with the equilibrium periods of the polymers. Several groups have investigated the effect of lateral confinement on the ordering of block copolymer thin films, both experimentally and numerically. Cheng and co-workers[30] observed stretching and compressing of the microdomain spacing perpendicular to the trench edges to match the trench width. They also found that larger wavelength undulations in the sidewalls lead to varying numbers of rows, with dislocations present where the number of rows changes. Sundrani et al. have studied the growth mechanism for alignment in the trenches.[25,26] They observed that one or two domains initially align along the edges of the trenches. On continued annealing, alignment parallel to the trench edges begins to grow at various spots along the length of the trench. The domains with perfect alignment grow with further annealing to assimilate less perfect regions until the alignment persisted along the entire length of the trenches. Using SCFT, Takahashi et al. have investigated the effect of commensurability on the equilibrium defect densities as well as kinetic rates for defect annihilation.[31] However, all of these studies have focused on confinement imposed by constant-width templates. A large number of templates must be prepared in order to ascertain a full picture of the effect of channel width on the assembly process. Here, we simplify this matter by employing wedges, with gradually changing channel width, to guide the self-assembly of block copolymer thin films.

In this study, we have investigated the alignment of cylinder-forming diblock copolymer thin films in such wedges. As a wedge turns from narrow to wide, polymer chains in a given number of cylinders would undergo expansion until a dislocation is introduced. The equilibrium positions for dislocations are determined both experimentally and theoretically. At the narrow end of the wedge, smaller confinement

Received: May 3, 2014
Revised: June 7, 2014
Published: June 16, 2014

   dx.doi.org/10.1021/ma500911y | *Macromolecules* 2014, 47, 4236−4242

widths impose powerful guiding fields for templating domain alignment. As a result, the deviations of dislocations from their equilibrium positions at the narrow end are smaller than those at the wide end of the wedges. Finally, the fluctuations of dislocations across the wedge are studied.

EXPERIMENTAL SECTION

A poly(styrene-*block*-methyl methacrylate) (PS-*b*-PMMA) block copolymer, obtained from Polymer Source, Inc., of Dorval, Quebec, was used in which PMMA forms cylindrical domains with a PS matrix. The molecular weight was 77 kg/mol with 29 wt % PMMA.

The silicon nitride substrates were spin-coated with a thin layer of PMMA photoresist and baked in air at 175 °C for more than an hour. A thin layer of Cr (70 Å) was then deposited onto the substrate using a homemade evaporator. The topographic patterns were prepared by electron beam lithography using a Hitachi S-2700 scanning electron microscope. After exposure, the films were developed in Cr etchant and then in a 1:3 mixture of methyl isobutyl ketone and isopropyl alcohol, rinsed extensively with isopropyl alcohol, and dried with nitrogen. The resulting patterns in the photoresist were converted into the topographic structures on the substrates by using a 95% CF_4 and 5% O_2 plasma etch. The remaining photoresist was removed by placing the substrates in acetone overnight. The nanochannels created in this manner were about 50 nm deep, and the opening angles of the wedges used in this study were from 1.5° to 4.5°.

The nanopatterned substrates were cleaned with toluene, acetone, and methanol using an ultrasonic cleaner and dried with nitrogen. The washed substrates were spin-coated with PS-*b*-PMMA block copolymer in 0.9% toluene solution at 4000−5500 rpm for 60 s and then preannealed at 523 K under an argon atmosphere.

RESULTS AND DISCUSSION

Alignment of Cylinder Domains in the Wedge. When a block copolymer thin film is spin-coated onto the nanopatterned substrate, polymer chains flow from the crests into the nanochannels upon annealing, leaving a featureless wetting layer on the crests. Copolymer accumulates inside the channels and phase separation occurs on the nanometer scale.[26,32] The wedges are filled with a layer of PMMA cylinders, which show fingerprint structures.

Figure 1a presents an AFM phase image of the alignment of cylindrical domains inside the wedge. PMMA interacting preferentially with the wedge sidewalls drives the alignment of cylindrical domains parallel to the edges of the wedges. Unlike in the nanochannels with a fixed width, the number of cylindrical domains change gradually in the wedge having a gradient in channel width. As the channel becomes progressively wider, the periodicity of the block copolymer domains deviates from the equilibrium periodicity of the unconfined domains (d_0). The ordered copolymer domains maintain a fixed number of cylinders by expansion. However, when the energetic cost of chain deformation becomes too high, a dislocation will be introduced, with an additional cylinder introduced into the cylinder arrays. The arrows in Figure 1a correspond to the positions of the dislocations. The dislocations are expected to be introduced at an equal interval $\Delta x = d_0/\tan\alpha \approx d_0/\alpha$, where α is the opening angle of the wedge.

Figure 1b shows the number of cylinder domains versus the measured confinement width W expressed in term of d_0. W is the effective width of the wedge, determined by the physical channel width minus the thickness of the two PMMA brush wetting layers that form at the surface of the substrate. (The average thickness of the brush layer is determined to be 42.0 nm from AFM images.) For each number of cylinder arrays N, the maximum and minimum confined widths are plotted. Here, the samples have been annealed at 523 K for 24 h to reach their equilibrium structures. It is observed that for a given number of cylinder arrays N, they occupy the confined region with the confinement width from $(N - 0.5)d_0$ to $(N + 0.5)d_0$. At the narrow end of this region, polymer chains are under compression, whereas at the wide end, polymer chains are under expansion. The transition in the number of cylinders from N to $N + 1$ is observed to occur when $W \approx (N + 0.5)d_0$.

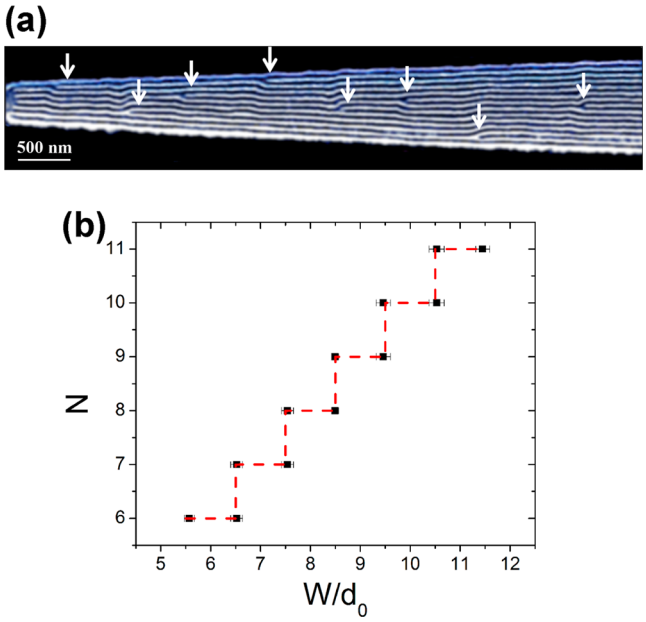

Figure 1. Alignment of cylinder-forming PS-*b*-PMMA block copolymer thin film in the wedge. (a) AFM phase image of ordered block copolymer domains in the wedge. Dislocations indicated by the white arrow occur periodically along the channel length. The sample was annealed at 250 °C for 24 h. (b) Number of cylinder domains, N, plotted against the confinement width, W, expressed in term of d_0, where d_0 is the equilibrium periodicity of the unconfined domains. The black dots indicate the positions where the dislocations are observed to be introduced. The transition in the number of cylinders from N to $N + 1$ is observed to occur when $W \approx (N + 0.5)d_0$.

Theoretically, the equilibrium position of the dislocation can be determined by minimizing the free energy of a confined region of width Nd_0 on the left side and $(N + 1)d_0$ on the right side, as illustrated in Figure 2. The direction along the wedge is defined as the x-axis, while the direction across it is defined as the z-axis. Let a dislocation, which transits the number of cylinders from N to $N + 1$, be located at the position where the

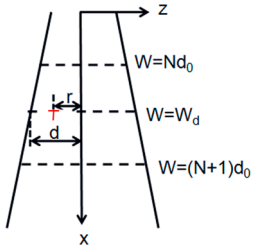

Figure 2. Geometry of a wedge. Dislocations are indicated by the red "T". The direction along the wedge is defined as the x-axis, while the direction across it is defined as the z-axis. r is the distance of the dislocation from the midplane of the wedge, and d is the distance from the midplane to the edge.

dx.doi.org/10.1021/ma500911y | *Macromolecules* 2014, 47, 4236−4242

width of edge equals to W_d. Dislocations separate the regions of compression and expansion of cylindrical domains. Between the region of the width Nd_0 and W_d, the polymer domains are expanded, while between the region of the width W_d and $(N + 1)d_0$, the polymer domains are compressed. It is known that the free energy per polymer chain of the confined cylindrical domains, $E_c(W,N)$, is approximated as $E_c(W,N)/E_0 = (1/3)[(W/Nd_0)^2 + 2Nd_0/W]$, where E_0 is the free energy per chain of the unconfined bulk block copolymer.[30] Therefore, the average free energy of polymer chains $\langle E_c(W_d,N/N+1)\rangle$ within the confined region between the width of Nd_0 and $(N + 1)d_0$ is

$$\langle E_c(W_d, N/N+1)\rangle = \frac{\int_{Nd_0}^{W_d} E_c(W, N)\mathrm{d}n(W) + \int_{W_d}^{(N+1)d_0} E_c(W, N+1)\mathrm{d}n(W)}{\int_{Nd_0}^{(N+1)d_0} \mathrm{d}n(W)} \quad (1)$$

where $\mathrm{d}n(W)$ is the number of the polymer chains occupy the confined widths from W to $W + \mathrm{d}W$.

$$\mathrm{d}n(W) = \frac{\rho N_A}{M} HW\frac{\mathrm{dW}}{\alpha} \quad (2)$$

where ρ and M are the density and molar mass of the polymer, N_A is Avogadro's number, and H is the thickness of the polymer film.

By plugging eq 2 into eq 1, $\langle E_c(W_d,N/N+1)\rangle$ is determined to be

$$\langle E_c(W_d, N/N+1)\rangle = \frac{2E_0}{3}\left\{\frac{4W_d^4}{[(2N+1)^2 - 1]^2 d_0^4} - \frac{2W_d}{(2N+1)d_0} + \frac{9}{4}\right\} \quad (3)$$

If we assume $(2N + 1)^2 - 1 \approx ((2N + 1)^2$ (such an assumption is reasonable in our studies, since the smallest N we measure is 6), then eq 3 can be written as

$$\langle E_c(W_d, N/N+1)\rangle = \frac{2E_0}{3}\left\{\frac{4W_d^4}{[(2N+1)d_0]^4} - \frac{2W_d}{(2N+1)d_0} + \frac{9}{4}\right\} \quad (4)$$

A plot of the average free energy $\langle E_c(W_d,N/N+1)\rangle$ is constructed for each value of N, as shown in Figure 3. The average free energy has its local minimum when the dislocation is at the equilibrium position. The width of the wedge at the equilibrium position for the dislocations, W_{de}, can be obtained by minimizing the free energy, $\partial\langle E_c(W_d, N/N+1)\rangle/\partial W_d = 0$.

$$W_{de} = \left(N + \frac{1}{2}\right)d_0 \quad (5)$$

The equilibrium positions for dislocations which transit the number of cylinders from N to $N + 1$ are where the width of wedge equals to $(N + 0.5)d_0$. This is consistent with the experimental results of Figure 1b.

Motion of Dislocations along the Wedge. Next, let us examine the motion of dislocations along the wedge, before they reach their equilibrium positions. Our high-temperature AFM enables us to probe real-time and real-space structure evolution directly.

Figure 4 shows the temporal evolutions of dislocations for different annealing times. Here, the sample has been

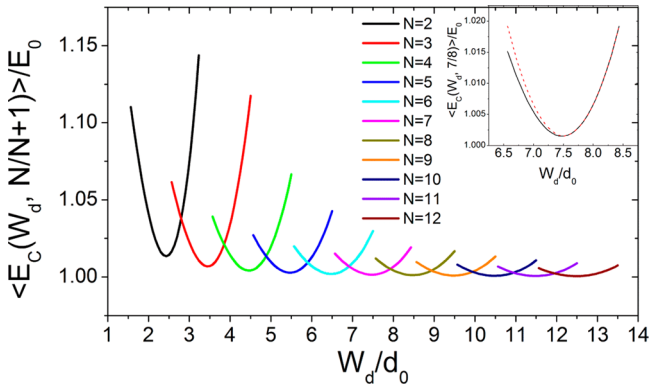

Figure 3. Average free energy $\langle E_c(W_d,N/N+1)\rangle$ plotted against the widths of the channel where the dislocations are introduced, W_d. The free energy is presented relative to the free energy of the bulk block copolymer. Inset: plots of the average free energy against the widths of the channel (solid line) and a perfectly symmetric curve of the free energy (dashed line). Here, we use $N = 7$ for an example. The two curves highlight the asymmetry of the free energy with regard to deviations from the equilibrium positions.

preannealed at 523 K for 2 h. The equilibrium positions for dislocations $W_{de} = (N + 1/2)d_0$ are indicated by the yellow dashed lines. The width differences between W_{de} and W_d and the distances dislocations travel along the wedge (Δx) at different annealing times are plotted in Figures 5a and 5b, respectively. Originally, at $t = 0$, the dislocations are located at the narrower end of the wedge, $W_d < W_{de}$, for all the values of N, as shown in Figures 4 and 5a. This behavior may result from the energy required to form a dislocation and the asymmetry of the free energy curve. As shown in the inset of Figure 3, the free energy increases more rapidly from the equilibrium positions at the wider end compared to the narrower end. It is, therefore, energetically more favorable for dislocations to form at the narrower end of the wedge $W_d < W_{de}$. And when the width of the wedge W is smaller than the equilibrium width for dislocation W_{de}, the cylinder domains will keep compressed until the compression energy overweighs the energy required to subtract a row. This situation is also observed in previous experiment.[30]

Thermal annealing facilitates the microdomain rearrangement and drives the confined system to equilibrium. Since initially dislocations are located at the positions where $W_d < W_{de}$, the cylinder domains between W_d and W_{de} are compressed. The compression stresses act on the dislocations a restoring force, which causes dislocations to translate to their equilibrium positions.[33,34] This behavior is observed in the subsequent images of Figure 4, in which the dislocations move to the wide end of wedge to relax the imposed compression. The width differences between W_{de} and W_d are decreased as shown in Figure 5a. Finally, all the dislocations move back to the equilibrium positions $W_d = W_{de}$ in Figures 4 and 5a, and the energy of block copolymer reaches the minimum. The dislocations will stay at their equilibrium positions with further increase of annealing time.

We also notice that the dislocations at the wide end of channel move a longer distance than the ones at the narrow end as shown in Figure 5b. For example, the dislocation which transits the number of cylinders from 12 to 13 has moved a distance of ~550 nm to reach the equilibrium position, while the dislocation which transits the number of cylinders from 6 to 7 has only moved a distance of ~250 nm. This is because that

dx.doi.org/10.1021/ma500911y | Macromolecules 2014, 47, 4236−4242

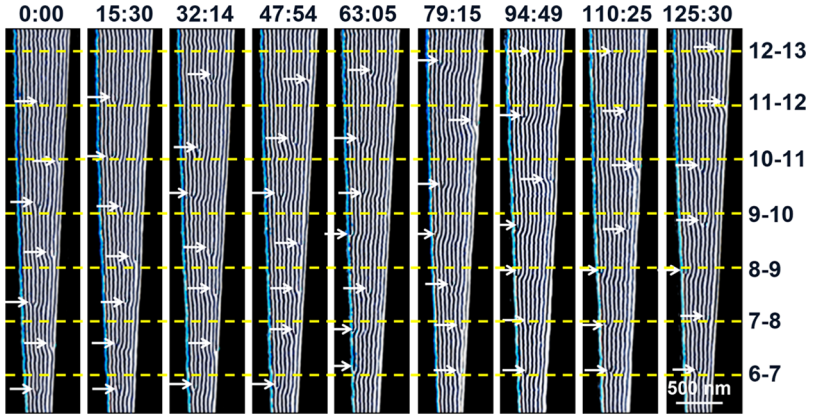

Figure 4. Time sequence of AFM phase images showing the motion of dislocations along the wedge. The dislocations are indicated by the white arrows. The number at the top of each image indicates the time (min:s) when the image is taken. The equilibrium positions for dislocations which transit the number of the cylinder domains from N to $N + 1$ are indicated by the yellow dashed lines. The images are taken at 250 °C. Originally, at $t = 0$, dislocations are located at the narrower end of the wedge. Upon annealing, all the dislocations translate to their equilibrium positions.

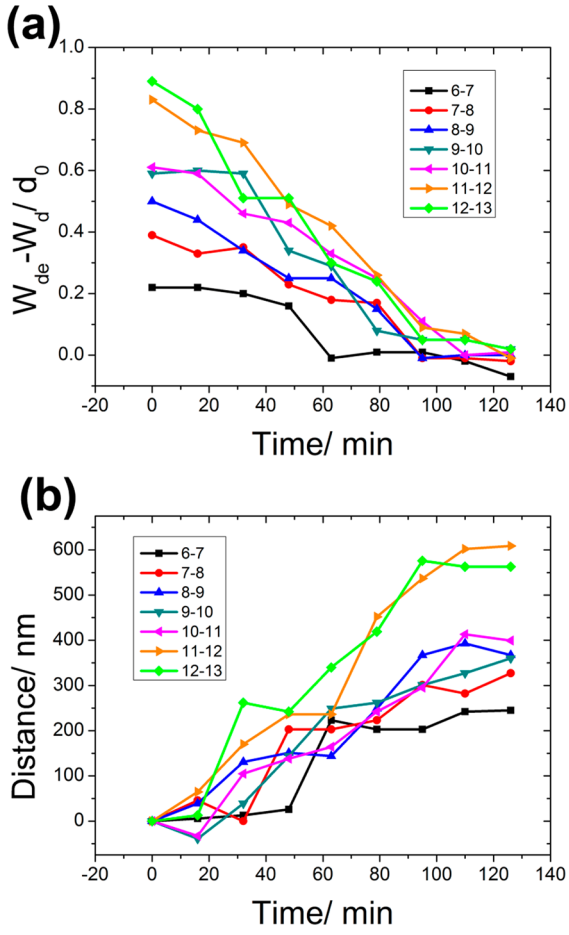

Figure 5. (a) Width differences between W_{de} and W_d, $W_{de} - W_d$ and (b) distances that dislocations move along the wedge, Δx, plotted against annealing time. Dislocations at the wide end of channel move a longer distance to their equilibrium positions than the ones at the narrow end because the latter dislocations do not significantly deviate from the equilibrium positions initially due to the stronger surface directing field from the sidewalls at the narrow end of the channel.

the former dislocation is farther away from its equilibrium position initially than the latter one. As shown in Figure 5a, at $t = 0$, the former dislocation is located at the place where $W_{de} - W_d$ equals $\sim 0.9d_0$, while for the latter dislocation, the width difference is only about $\sim 0.2d_0$. This behavior can be explained by the steeper energy minima at smaller confinement widths as shown in Figure 3. A slight deviation from the equilibrium value would result in large increase in the free energy of the system. Therefore, the dislocations at the narrower end of the wedge can not deviate from the equilibrium positions too much initially. As W increases, the energy minima become shallower, as the incommensurability at the wide end of the channel can be distributed over many cylinder domains, and the amount of distortion of each polymer domain is decreased. Therefore, a larger deviation from the equilibrium position for a given defect occurs initially for wider positions in the channel, and such dislocations at the wider end of the wedge move a longer distance to reach their equilibrium positions.

Motion of Dislocations across the Wedge. Lateral confinement of the wedge does not only determine the positions of dislocations in the x-axis, it also interacts with the dislocations in the z-axis. Previous simulation studies[35] show that in an ideal situation, where the two sidewalls are equally smooth, the dislocations form at the midplane of the wedge, which corresponds to the minimum-energy state. However, the roughness of the two side walls will move the dislocations toward the edges of the wedge. In accordance with the simulation results, we found, in our experiment, the possibilities of dislocations located near the two side walls of the wedge being larger than anywhere else in the wedge. The locations of dislocations in the z direction are quantified by the ratio r/d, where r is the distance of the dislocation from the midplane of the wedge and d is the distance from the midplane to the edge, as is shown in Figure 2. When the positions of dislocations are at the edge of the wedge, r/d equals 1, while when the positions of dislocations are at the central line of the wedge, r/d equals 0. Figure 6 is the histogram of the positions of dislocations for transitions from N to $N + 1$. At least 300 dislocations for each transition were analyzed in samples annealed at 250 °C for 12 h. It is observed that the probabilities for the ratio r/d close to 1 are larger than those for any other values, which means that the probabilities of dislocations being located near the edge of the wedge are larger than anywhere else in the wedge. This behavior is more obvious at the narrow end of the wedge. As shown in Figure 6, for transition from 6 to 7, the probability of ratio r/d close to 1 is almost 60%, while for transition from 12 to 13, the probability drops to around 25%. This is because that

dx.doi.org/10.1021/ma500911y | Macromolecules 2014, 47, 4236−4242

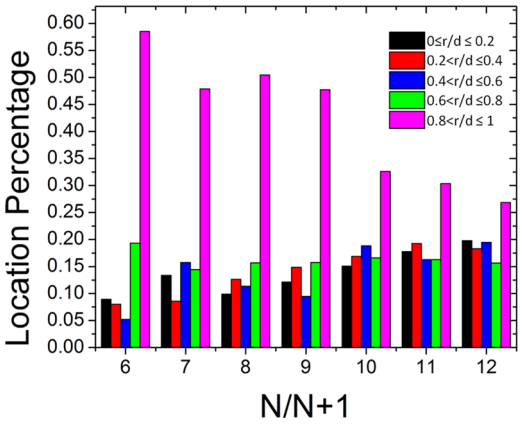

Figure 6. Histogram of the positions of dislocations across the wedge. The probabilities of dislocations located near the edge of the wedge are larger than anywhere else in the wedge. However, dislocations can move freely in the central region of the wedge.

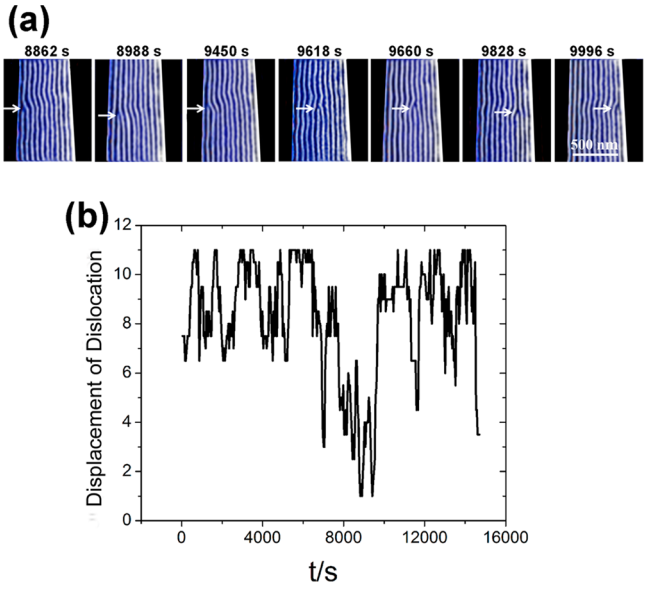

Figure 7. (a) AFM phase image series showing the fluctuation of dislocations across the wedge. The dislocations are indicated by the white arrows. The number at the top of each image indicates the time when the image is taken. All the images are taken at 245 °C. (b) Displacement versus t curve of the fluctuating dislocations in (a). The trajectory further indicates that the dislocations can move freely across the wedge.

as the wedge becomes wider, the percentage of the surface area near the edge over all the surface area inside the wedge decreases. We find, in experiment, when a dislocation reaches the two cylinder domains next to the side walls, it is very likely it will be pinned there. Therefore, for transition from 6 to 7, the percentage of the surface area near the edge over all the surface area is 4/7, while for transition from 12 to 13, the percentage decreases to 4/13. Therefore, as the wedge becomes wider, the probability of finding the dislocations located at the edge area decreases. We also note, except near the edge, that the probabilities of dislocations located in other areas in the wedge are evenly distributed, which means the dislocation can move freely in the central region of the wedge. This is consistent with previous experimental results, which indicate that there is little influence of the template contour on the positions of the polymer domains across the channel beyond one or two polymer rows next to the edges.[36]

After dislocations reach their equilibrium positions in the x direction, they will keep fluctuating inside the wedge. Next, we studied the motion of dislocations across the wedge, which is in the z direction. We only studied the dislocations at the wide end of the wedges, since the dislocations at the wide end of the wedges could move freely inside the wedges, while those at the narrow end of wedges are easily pinned to the two sidewalls.

We studied the motion of dislocations across the wedge under five different temperatures: 230, 235, 240, 245, and 250 °C. At each temperature, at least four trajectories for ~200 image frames are imaged with a time resolution of ~3 min from 230 to 240 °C, ~42 s at 245 °C, and ~21 s at 250 °C. As an example, a representative trajectory of dislocation at 245 °C is shown in Figure 7. Here, we focus on the dislocations which transit the number of cylinder domains in the wedge from 10 to 11. Fluctuation behaviors of dislocations across the wedge are visible in the AFM sequential images, as shown in Figure 7a. In Figure 7b, we plot the displacements for dislocations over a time period of ~4 h. The cylinder domains are numbered as 1, 2, ..., 11 from left to right. If the displacement is 4 on the trajectory, it means that the dislocation is located at the fourth cylinder domain counted from left to right. The trajectories further indicate that the dislocations can move freely across the central region of the wedge.

Quantitative analysis of z positions of the dislocations with time was carried out to obtain more information about the fluctuation behavior of the dislocations. The one-dimensional mean-square displacement MSD($n\Delta t$) as a function of the time interval of $n\Delta t$ is calculated according to the formula[37,38]

$$\mathrm{MSD}(t) = \mathrm{MSD}(n\Delta t) = \frac{\sum_{i=1}^{N-n} (z_{i+n} - z_i)^2}{N - n} \tag{6}$$

where z is the position of the dislocation in the z-axis, N is the total number of positions measured, n is the measurements index going from 1 to N, and Δt is the time interval between two consecutive images. For simple 1-dimensional Brownian motion, $\mathrm{MSD}(n\Delta t) = 2D_z n\Delta t$, where D_z is 1-dimensional diffusion coefficient. The MSD$-n\Delta t$ plot is linear with a slope of $2D_z$. In our experiments, the motion of dislocation is confined diffusion, since the dislocations move inside the wedge and cannot move out of the area. For confined diffusion, the MSD$-n\Delta t$ plot is downward curved with an asymptotic approach to a finite MSD value, which can be expressed as[37−39]

$$\mathrm{MSD}(t) = \mathrm{MSD}(n\Delta t) = A(1 - \mathrm{e}^{-n\Delta t/\tau})$$
$$A = \frac{L_z^2}{6} \tag{7}$$

where L_z is the length in the z direction that a dislocation can move ($0 \le z \le L_z$) and τ is the equilibration time. The initial slope of the MSD curve at $t = 0$ is $2D_z$; then

$$D_z = \frac{A}{2\tau} \tag{8}$$

In Figure 8a, the MSD$-n\Delta t$ curves at the five temperatures studied are fitted using eq 7, and the resultant values of A, τ, and D_z are shown in Table 1. As expected, the plot is downward curved with an asymptotic approach to $L_z^2/6$. The diffusion coefficients D_z is defined by the initial slopes. When the dislocations reach the sidewall of the wedge, it is very likely that

dx.doi.org/10.1021/ma500911y | Macromolecules 2014, 47, 4236−4242

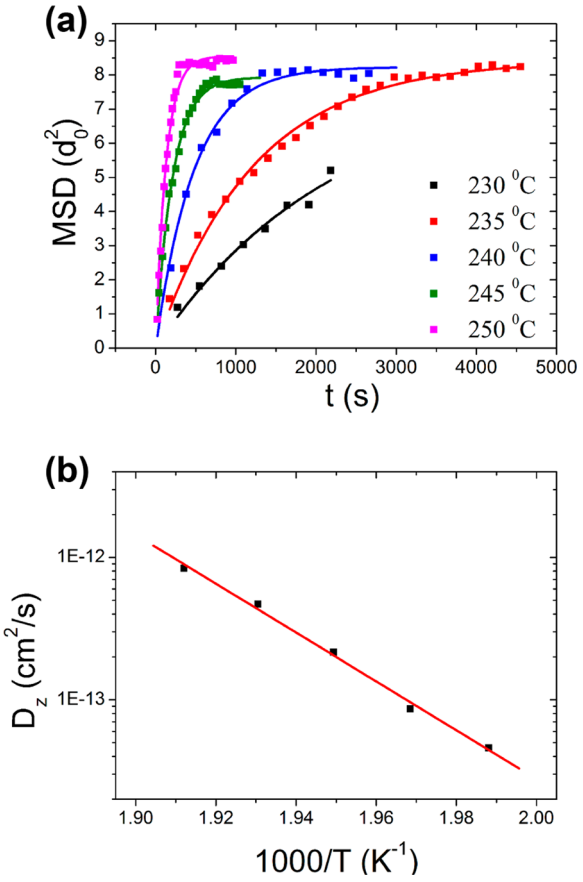

Figure 8. (a) MSD plots from dislocations trajectories taken at 230, 235, 240, 245, and 250 °C. The solid lines are the best fits of eq 7. (b) Arrhenius plot of the diffusion coefficients obtained from (a). The diffusion activation energy is determined to be E_A = 328 ± 13 kJ/mol.

Table 1. Parameters Used To Fit MSD Curves and the Diffusion Coefficients Determined

temp (°C)	A (d_0^2)	τ (s)	D_z (10^{-13} cm^2/s)
230	7.8	2176	0.45
235	8.5	1234	0.86
240	8.2	478	2.16
245	8.0	212	4.68
250	8.5	129	8.30

they will be pinned to the surface. Hence, we eliminate the points from the trajectories when the dislocations are located at the two cylinder domains next to each side walls. Then the distance in the z direction that dislocations for transition from 10 to 11 cylinders can move L_z is $7d_0$. $A = L_z^2/6 = 8.2\ d_0^2$, which is consistent with our fitting results. It further indicates that the dislocations can move freely across the central wedge. As temperature increases, the equilibration time decreases dramatically, as a result of the increase of the diffusion coefficient D_z, which is given by $D_z = A/2\tau$. The values of diffusion coefficients agree with perpendicular diffusion coefficients D_{perp} determined from previous experiments.[28] The temperature dependence of diffusion coefficients (D_z) is plotted in Figure 8b. The observed temperature dependence follows an Arrhenius law with the activation energy of E_A = 328 ± 13 kJ/mol, which compares well with previous measurements of 377 kJ/mol for 84 kg/mol[40] and 270 kJ/mol for 64 kg/mol[41] cylinder-forming PS-*b*-PMMA thin film.

SUMMARY

Patterned tapered nanochannels of linearly varying width have been used to template cylindrical block copolymer microdomains. Dislocations occur periodically along the channel length. Movements of dislocations along and across the channels are observed using *in situ* high-temperature AFM imaging with environmental control. The widths of the channel at the equilibrium positions of dislocations, which transit the number of cylinders from N to $N + 1$, are determined to be $(N + 0.5)d_0$ from both experiments and calculations. Upon annealing, all dislocations move to and reach their equilibrium positions. At the narrow end of the channel, confinement imparts a stronger directing field on the alignment of block copolymer domains, and consequently, dislocations cannot deviate significantly from their equilibrium positions. However, at the wider end, incommensurability is distributed over many cylinder domains, and large deviation is allowed. Finally, the fluctuations of dislocations at the equilibrium positions were studied, and the perpendicular diffusion coefficients and activation energy are obtained. These experiments clearly demonstrate the ability to control the placement of periodically located dislocations along tapered nanochannels, offering an efficacious route to placing defects at predetermined locations in such hierarchically assembled nanostructures. This also suggests the possibility of transporting and concentrating defect-seeking species such as nanoparticle additives into intentionally selected locations along the tapered channel.

AUTHOR INFORMATION

Corresponding Author

*E-mail: s-sibener@uchicago.edu (S.J.S.).

Present Address

Q.Z.: Morningstar Inc., Chicago, IL, 60602.

Notes

The authors declare no competing financial interest.

ACKNOWLEDGMENTS

This work was supported by DTRA under Grant HDTRA1-11-1-0001. It is also a pleasure to acknowledge partial support from the Materials Research Science and Engineering Center at The University of Chicago, NSF-DMR-0820054.

REFERENCES

(1) Park, M.; Harrison, C.; Chaikin, P. M.; Register, R. A.; Adamson, D. H. *Science* **1997**, *276* (5317), 1401−1404.
(2) Rachel, A. S. *Mater. Sci. Eng., R* **2005**, *48* (6), 191−226.
(3) Park, C.; Yoon, J.; Thomas, E. L. *Polymer* **2003**, *44* (22), 6725−6760.
(4) Sohn, B. H.; Seo, B. H. *Chem. Mater.* **2001**, *13* (5), 1752−1757.
(5) Watkins, J. J.; McCarthy, T. J. *Chem. Mater.* **1995**, *7* (11), 1991−1994.
(6) Kim, H. C.; Jia, X.; Stafford, C. M.; Kim, D. H.; McCarthy, T. J.; Tuominen, M.; Hawker, C. J.; Russell, T. P. *Adv. Mater.* **2001**, *13* (11), 795−797.
(7) Thurn-Albrecht, T.; Schotter, J.; Kästle, G. A.; Emley, N.; Shibauchi, T.; Krusin-Elbaum, L.; Guarini, K.; Black, C. T.; Tuominen, M. T.; Russell, T. P. *Science* **2000**, *290* (5499), 2126−2129.
(8) Thurn-Albrecht, T.; DeRouchey, J.; Russell, T. P.; Kolb, R. *Macromolecules* **2002**, *35* (21), 8106−8110.
(9) Amundson, K.; Helfand, E.; Quan, X.; Hudson, S. D.; Smith, S. D. *Macromolecules* **1994**, *27* (22), 6559−6570.
(10) Morkved, T. L.; Lu, M.; Urbas, A. M.; Ehrichs, E. E.; Jaeger, H. M.; Mansky, P.; Russell, T. P. *Science* **1996**, *273* (5277), 931−933.

(11) Angelescu, D. E.; Waller, J. H.; Adamson, D. H.; Deshpande, P.; Chou, S. Y.; Register, R. A.; Chaikin, P. M. *Adv. Mater.* **2004**, *16* (19), 1736−1740.
(12) Kimura, M.; Misner, M. J.; Xu, T.; Kim, S. H.; Russell, T. P. *Langmuir* **2003**, *19* (23), 9910−9913.
(13) Petermann, J.; Gohil, R. M. *J. Mater. Sci.* **1979**, *14* (9), 2260−2264.
(14) Park, C.; De Rosa, C.; Thomas, E. L. *Macromolecules* **2001**, *34* (8), 2602−2606.
(15) Chen, H. *J. Chem. Phys.* **1998**, *108* (16), 6897.
(16) Pereira, G. G.; Williams, D. R. M. *Macromolecules* **1999**, *32* (3), 758−764.
(17) Rockford, L.; Liu, Y.; Mansky, P.; Russell, T. P.; Yoon, M.; Mochrie, S. G. J. *Phys. Rev. Lett.* **1999**, *82* (12), 2602−2605.
(18) Ouk Kim, S.; Solak, H. H.; Stoykovich, M. P.; Ferrier, N. J.; de Pablo, J. J.; Nealey, P. F. *Nature* **2003**, *424* (6947), 411−414.
(19) Park, S.-M.; Craig, G. S. W.; Liu, C.-C.; La, Y.-H.; Ferrier, N. J.; Nealey, P. F. *Macromolecules* **2008**, *41* (23), 9118−9123.
(20) Segalman, R. A.; Yokoyama, H.; Kramer, E. J. *Adv. Mater.* **2001**, *13* (15), 1152−1155.
(21) Segalman, R. A.; Hexemer, A.; Kramer, E. J. *Phys. Rev. Lett.* **2003**, *91* (19), 196101.
(22) Segalman, R. A.; Hexemer, A.; Kramer, E. J. *Macromolecules* **2003**, *36* (18), 6831−6839.
(23) Kim, S. H.; Misner, M. J.; Xu, T.; Kimura, M.; Russell, T. P. *Adv. Mater.* **2004**, *16* (3), 226−231.
(24) Black, C. T.; Bezencenet, O. *IEEE Trans. Nanotechnol.* **2004**, *3* (3), 412−415.
(25) Sundrani, D.; Darling, S. B.; Sibener, S. J. *Langmuir* **2004**, *20* (12), 5091−5099.
(26) Sundrani, D.; Darling, S. B.; Sibener, S. J. *Nano Lett.* **2003**, *4* (2), 273−276.
(27) Park, S. M.; Stoykovich, M. P.; Ruiz, R.; Zhang, Y.; Black, C. T.; Nealey, P. F. *Adv. Mater.* **2007**, *19* (4), 607−611.
(28) Tong, Q.; Sibener, S. J. *Macromolecules* **2013**, *46* (21), 8538−8544.
(29) Ryu, H. J.; Tong, Q.; Sibener, S. J. *J. Phys. Chem. Lett.* **2013**, *4* (17), 2890−2895.
(30) Cheng, J. Y.; Mayes, A. M.; Ross, C. A. *Nat. Mater.* **2004**, *3* (11), 823−828.
(31) Takahashi, H.; Laachi, N.; Delaney, K. T.; Hur, S. M.; Weinheimer, C. J.; Shykind, D.; Fredrickson, G. H. *Macromolecules* **2012**, *45* (15), 6253−6265.
(32) Sundrani, D.; Sibener, S. J. *Macromolecules* **2002**, *35* (22), 8531−8539.
(33) Oswald, P.; Kleman, M. *C. R. Acad. Sci., Ser. II* **1982**, *294* (17), 1057−1060.
(34) Smalyukh, I. I.; Lavrentovich, O. D. *Phys. Rev. E* **2002**, *66* (5), 051703.
(35) Qian, H. Striped pattern formation in geometrically constrained systems. Dissertation, the University of Chicago, Ann Arbor, ProQuest/UMI, 2007; pp 43−51.
(36) Cheng, J. Y.; Zhang, F.; Smith, H. I.; Vancso, G. J.; Ross, C. A. *Adv. Mater.* **2006**, *18* (5), 597−601.
(37) Daumas, F.; Destainville, N.; Millot, C.; Lopez, A.; Dean, D.; Salome, L. *Biophys. J.* **2003**, *84* (1), 356−366.
(38) Jin, S.; Verkman, A. S. *J. Phys. Chem. B* **2007**, *111* (14), 3625−3632.
(39) Sako, Y.; Kusumi, A. *J. Cell Biol.* **1994**, *125* (6), 1251−1264.
(40) Hahm, J.; Sibener, S. J. *J. Chem. Phys.* **2001**, *114* (10), 4730−4740.
(41) Ruiz, R.; Bosworth, J. K.; Black, C. T. *Phys. Rev. B* **2008**, *77* (5), 054204.